Mapping multi-contrast microstructural MRI of the placenta

Baptiste Moalic, SN: 22182376, University College London[1]

[1]**UCL, Gower Street, WC1E 6BT, London, UK**

ABSTRACT

We will use multi-contrast MRI to see if we can find differences between a healthy and an ill placenta (here suffering from pre-eclampsia). After having fitted both simple and more complex models, we can say that we can observe symptoms from early stages with this MRI data: more basic models like T_2^*-ADC and T_2^*-IVIM already show differences in the relaxation time T_2^*, and anisotropic models like the zeppelin-zeppelin and stick-ball-sphere show a change of micro-structure for the pre-eclampsia patient that could explain why the placenta does not work as intended.

Keywords: multi-contrast MRI, placenta, pre-eclampsia, relaxation time T_2^*, anisotropic compartment models, diffusion imaging

INTRODUCTION

The placenta is an organ that plays a fundamental role during pregnancy: it is in charge of the exchange of nutrients between the mother and the fetus, and more importantly of the circulation of oxygenated blood. Therefore, a complication in this area could have detrimental effects on the fetus. Also, the sooner we are able to identify such problems, the better we will be able to handle this, and the lower the risks for both the unborn child and her mother.

Here, we focus mainly on the pre-eclampsia condition. Why would we develop an imaging technique for this disease? Women suffering from pre-eclampsia often do not show any symptoms (Mol et al., 2016), therefore clinicians have to rely on techniques assessing the blood of the patient, and biochemical tests to test the renal functions for example. This is a painful process for the mother, especially when we know that the main solution to prevent pre-eclampsia from doing more damage is to deliver the baby. Thus, delivery time must be optimal, so the mother must be closely monitored and frequently tested to assess this in the best way possible. Moreover, signs of pre-eclampsia often reveal themselves when the disease has reached a mild to severe stage. All in all, timing is essential, and the less disturbed the patient is, the best for her. That is why the recent advances in T_2^* relaxometry and diffusion-weighted imaging (DWI) - which are non-invasive techniques - can prove to be a real improvement for the identification and treatment of pre-eclampsia. DWI for the circulation of the fluids, and T_2^* relaxometry for the level of oxygen in the blood.

What has already been done in placental imaging surrounds fitting models to identify the microstructure of the placenta (Melbourne et al., 2018) (Slator et al., 2018), and simple models to discriminate between healthy and ill placentas (Slator et al., 2019). What we aim to do here, is to see if we can highlight differences between pre-eclampsia placentas and normal ones, but with more complex models. We will start by describing the method we have followed and the data we have used. Then, we will present our results and discuss them. Finally, we will try to identify the future directions we could take following our conclusions.

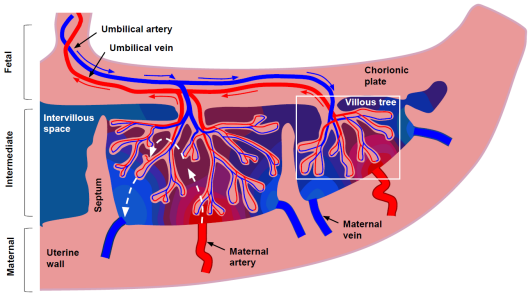

Figure 1. Schematic of the placenta

METHODS AND DATA

Data and MRI acquisition parameters

As the title of this article suggests, we will work on two multi-contrast diffusion MRI scans: one from a healthy control, and one from a participant who went on to be diagnosed with pre-eclampsia. As well as the MRI volumes, we are given binary masks, representing the region of interest (ROI) we need to explore. This is important because the placenta is surrounded by other structures and organs, and during scanning the patient breathes, and placental imaging is sensitive to the changes induced by this movement. Therefore, we need to be cautious about the area we process in our models. Let's note that our ROI includes both the placenta and the uterine wall: because we are interested in identifying the areas of exchanges between the placenta and outside of it, the uterine wall can play a role in the circulation of blood and nutrients.

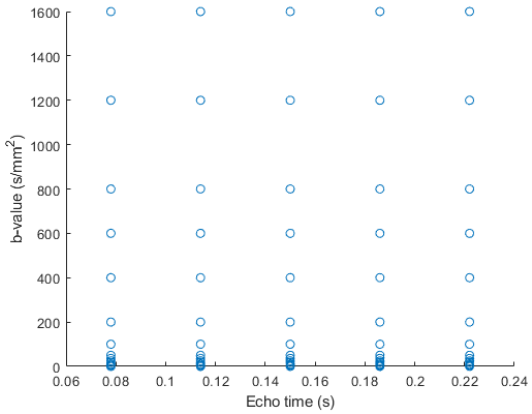

Figure 2. Acquisition parameters for our MRI volumes: echo times and b-values

What does multi-contrast mean for our MRI scans? It means that we have both the diffusion weighting information: b-values (in s/mm^2) and gradient directions, and the T_2^* relaxometry-related information: echo times (in s). The acquisition process is shown in Figure 2. As displayed, for each echo time, we will have different corresponding b-values. We can note that there are more acquisitions with low b-values, because this parameter is contained in a decreasing exponential, so the higher it is, the weaker the output signal is. To end this part, here are some examples of the data we will be using. The scans are comprised of 4 dimensions: x, y, z, and acquisition parameters. We can see in Figure 3a that we can go through the z dimension (first row) and through the echo time/b-value dimension (second row). In Figure 3b, we display the masks marking the placenta and uterine wall out from the rest of the body.

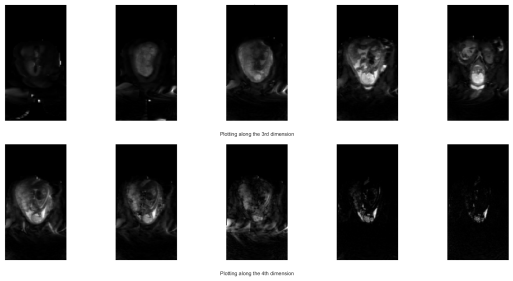

(a) Placenta scans. We show some examples along the z dimension (first row) and along the acquisition parameters dimension (second row)

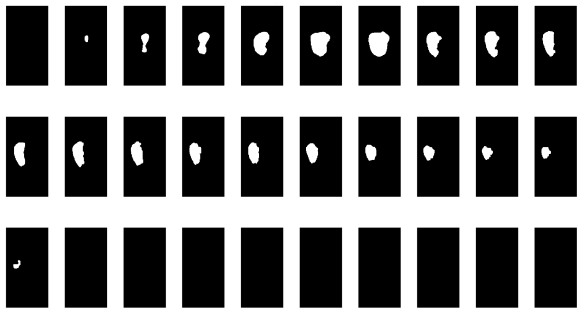

(b) Binary masks defining the limits of the placenta and the uterine wall combined

Figure 3. Example of data we will use in the context of this article (both from the healthy subject)

Models to fit

We want to know if there is a way to distinguish a sane placenta from an ill placenta. To do so, we have to extract information from our data: this is parameter mapping. The main parameters we will estimate in our models are the T_2^* relaxation time and the diffusivity/pseudo-diffusion coefficients D.

As a first estimation, we will use the T_2^*-ADC and T_2^*-IVIM models described in (Slator et al., 2019):

- T_2^*-ADC: $S = S_0 \exp(\frac{-TE}{T_2^*}) \exp(-bD)$
- T_2^*-IVIM: $S = S_0 \exp(\frac{-TE}{T_2^*})[f \exp(-bD_p) + (1-f)\exp(-bD)]$

where S_0 is the first value for the fourth dimension (parameter acquisitions, i.e a b-value of 0 and an echo time of 78ms) for the voxel in question, TE is the echo time, and b is the b-value.

We do not expect these models to give us the perfect fit, but rather a first estimate of our parameters of interest. We can see that they are isotropic models, and that will prove not to be the best choice in the following. This is also backed by the fact that in (Slator et al., 2018), the models that performed better were the anisotropic-isotropic and anisotropic-anisotropic ones.

Therefore, we will try extended-compartment models. They can be found in Table 1 of (Slator et al., 2018). In the set of models, we can find isotropic-isotropic (e.g Ball-Ball), anisotropic-isotropic (e.g Stick-Ball), isotropic-anisotropic (e.g Ball-Zeppelin), and anisotropic-anisotropic models (e.g Zeppelin-Zeppelin). The different shapes of each compartment will enable us to discover the structure of the perfusing and diffusing parts within the placenta.

Our extended-compartment models will have the general following form:

$$S = S_0 \exp\left(\frac{-TE}{T_2^*}\right) \sum_{i=0}^{3} f_i S_i \qquad \text{with} \quad \sum_{i=0}^{3} f_i = 1$$

where the formulae for each S_i compartment can be found in (Panagiotaki et al., 2012). Contrary to (Slator et al., 2018), our likelihood model is not Rician but Gaussian, for simplicity.

Finally, we will also investigate the T_2^*-D spectrum (done in (Slator et al., 2019) with an inverse Laplace transform), using the following discretized signal expression:

$$S = \sum_{i=1}^{N_{T_2^*}} \sum_{j=1}^{N_D} F(T_{2i}^*, D_j) \exp\left(\frac{-TE}{T_{2i}^*}\right) \exp\left(-bD_j\right)$$

where $N_{T_2^*}$ and N_D are respectively the number of T_2^* and D we use for the grid of values. This will give us a new way of visualizing the parameters, rather than on a map, and we will also use other optimization tools.

Methods of computation

We will use `fminunc` and `fmincon` functions from MATLAB (TheMathWorksInc., 2022). We give the starting vector of parameters, and the output of the function to be optimized is the sum of squared differences between the voxel data, and the voxel estimated with one of our models. Beforehand, we tested our functions on single random voxels with noise added to the starting vectors of parameters. `fminunc` resulted faster and almost as stable as `fmincon`, so we mainly used `fminunc`. `fmincon` was only used for the three-compartment models where we had to enforce the $\sum_{i=0}^{3} f_i = 1$ condition.

To be more certain of our results, for each voxel, we repeat the optimization process 2 to 5 times (depending on the performance of each model on single random voxels; we usually reach the global minimum in 2-5 iterations) adding noise to the starting vector of parameters.

Finally, as far as the starting values as concerned, we have used the data in Supporting Table S1 from (Slator et al., 2018) to get the boundary values, and the starting values are taken to be approximately in the middle of the boundary interval (plus noise at each repetition of the optimization process).

As for the continuum modelling (T_2^*-D spectrum), we will vectorize the double sum, taking values of T_2^* and D in the range indicated by our previous estimates (in our case, T_2^* between 0 and 125ms, D between 0 and 0.01mm^2/s). This will result in the following equation: $S = KF$ where S contains the mean signal value over all voxels for each ROI, K is the grid of T_2^* and D values that we sample ourselves and F is the vector of spectrum values. This is a linear least-squares problem with positive values only, we will then use MATLAB's `lsqnonneg`.

We can also mention that we will work on slice 7 (along the z-dimension) of the placenta scan, this slice should give us enough insight into what is happening inside the organ.

RESULTS

T_2^*-ADC and T_2^*-IVIM fitting

As mentioned earlier, to check if our method is likely to present results, we will first fit simpler models like T_2^*-ADC and T_2^*-IVIM (see above for the formulae). Our first results can be found in Figure 4. We have plotted

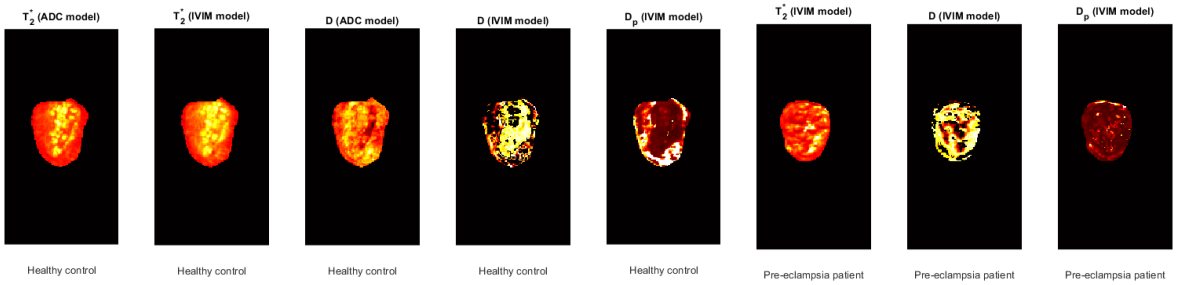

Figure 4. Fitting of the ADC and IVIM models for the slice 7. The parameter represented by the map can be found on top of each image, and the state of the patient (healthy or ill) can be found below the image.

both the ADC and IVIM models because looking at the D (ADC) versus D and D_p (IVIM) (plots 3-5 starting from the left), we can already see that the IVIM model discriminates between two areas: the core of the placenta and its boundaries/uterine wall. This is a motivation for our future extended compartments models.

Other than that, we can see that the T_2^* parameter maps look different, which is already an indication that they should not behave in the same way. We have normalized the map for visualization, therefore let's take a look at the boxplot of the T_2^* values from both maps.

In Figure 5, we can clearly observe that for the pre-eclampsia placenta, the T_2^* relaxation time is longer for a significant part of the voxels. Therefore, even quicker fittings like the ADC and IVIM models are able to give us reliable T_2^* values, which can allow us to see if the two placentas are different.

Unfortunately, when computing the BIC maps for the two patients, our results show that the IVIM model dominantly ends up as the most informative model. Except for the remark on D and D_p, it seems that these two simpler models are insufficient to explain the microstructure of the placenta. That is why we need to investigate new ways of fitting and displaying parameter information.

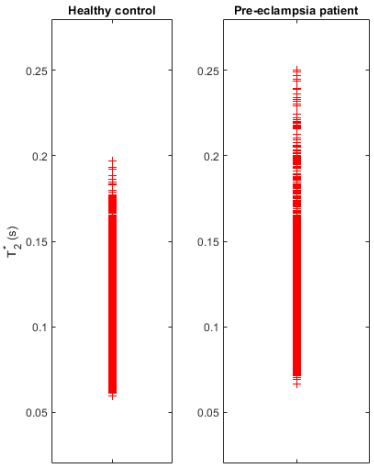

Figure 5. Acquisition parameters for our MRI volumes: echo times and b-values

Continuum modelling (T_2^*-D spectra)

By following the method explained in the previous section, we compute a contour map of the T_2^*-D spectrum. It is in Figure 6.

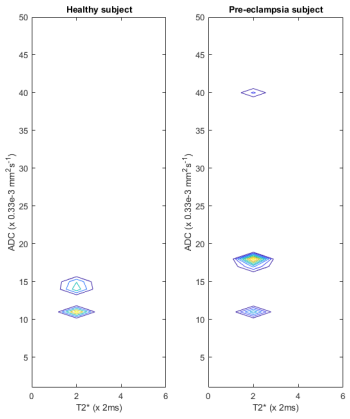

Figure 6. Contour map of the T_2^*-D spectrum, for healthy and pre-eclampsia patients

What comforts us in our methods, is that there are both similarities and differences in our contour plot. We will also accentuate the results found in (Slator et al., 2019) with their inverse Laplace transform.

Both graphs show a contour around 0.33e-2 mm^2/s, which should correspond to the diffusion of water in tissue. Both placentas keep that characteristic, although we can distinguish a difference in the contour itself. What changes is the spectrum value for higher diffusion coefficients. This emphasizes the fact that there is something that has happened to the circulation of fluids (e.g blood) in the organ. What is more telling is the third contour we can see on the right plot, showing that there is a decrease in diffusivity for the ill placenta. The multiple contours are yet another indication that the placenta is home to different compartment with fluids of different diffusivities going through them.

The T_2^*-D spectrum and its contour map can therefore be

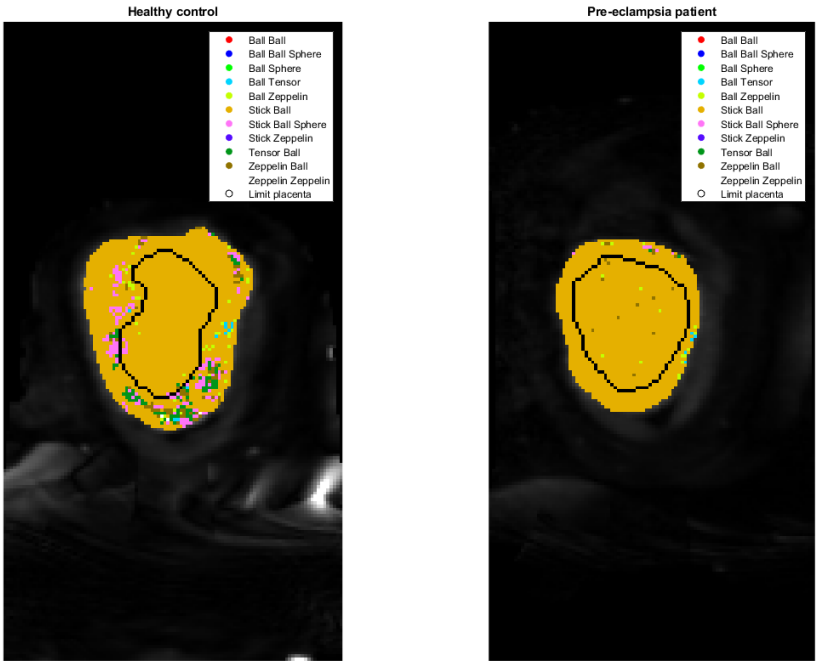

Figure 7. BIC maps for the healthy (left) and pre-eclampsia (right) patient. This is slice 7 of our placenta scans. Refer to the legend to identify the different models. The limit between the placenta and the uterine wall is represented by the black contour in the organ.

considered as another tool to identify placentas different from healthy controls. Besides, the contour map allows us to spot "areas" within the placenta where different fluids circulate.

Anisotropic extended compartments fitting

As described in the Methods section, we will now fit voxel-by-voxel new models to try to get a better understanding of the inner microstructure of the placenta. The models we will use are comprised of both anisotropic and/or isotropic compartments, they can be found in Table 1 of (Slator et al., 2018).

When fitting all of the 11 models, we find that the lowest BIC value for each voxel is always the one from the IVIM model (like in the first part of our Results section). We think it has to do with the method used. Indeed, `fminunc` is more subject to numerical instabilities than `fmincon`. Also, we have combined the exponential T_2^* factor with the exponential compartment models; this leads to smaller values, resulting in a greater risk of numerical errors. One major takeaway from (Slator et al., 2018) is that the models obtaining the best fit to the data are the aniso-iso and aniso-aniso ones. Therefore, we choose not to consider the iso-iso compartment models to focus only on the anisotropic ones, to see if we get closer to a result already known, considering that anyway, our method cannot produce lower error values for more complex models. The BIC maps can be found in Figure 7.

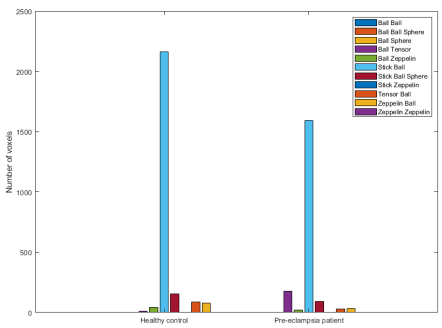

Figure 8. Histograms of the best-fitting models for each patient

Firstly, we can see that the placenta can in fact be explained by different anisotropic models. We can particularly observe this on the left plot. Mainly, different vessels of fluid circulation can be found at the boundary between the placenta and the uterine wall. This is expected, as seen in Figure 1 in the introduction: the arteries/veins and their crossroads surround the placenta. What about the inside of it though? Our model seems to only identify one best model, whereas the placenta schematic suggests

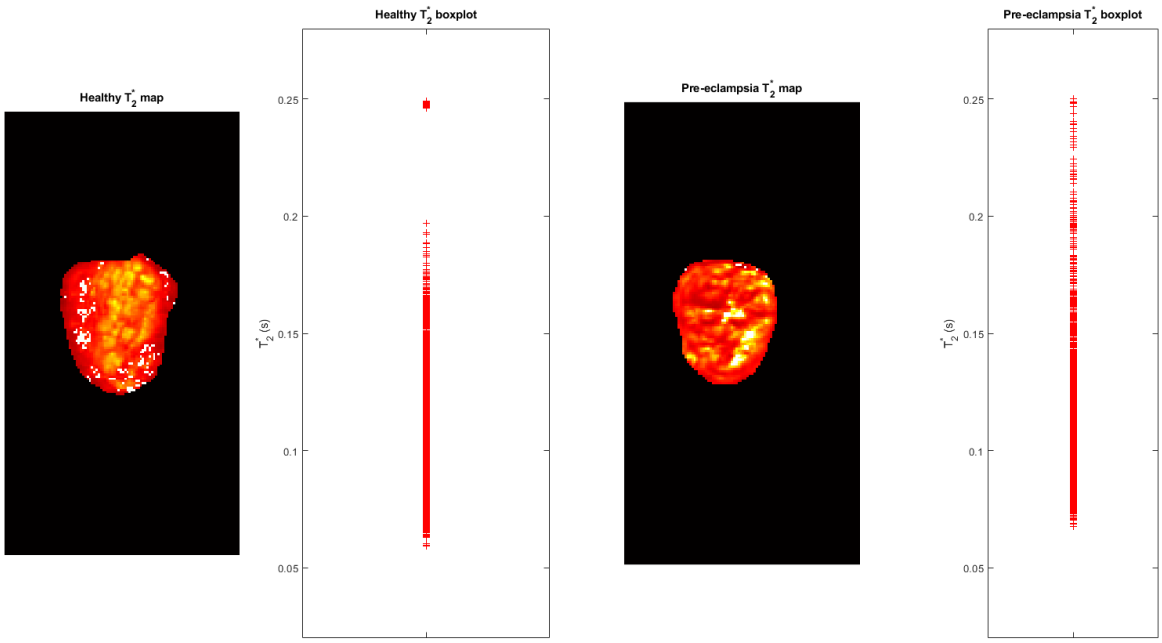

Figure 9. Maps (normalized) and boxplots representing the T_2^* values

more complex structures. Let's keep in mind that we have only studied a slice of the placenta and that one of the challenges of placental imaging is to make sense of multiple scans at the same time because the veins and arteries are not flat: they have to be followed through multiple z-dimensions. The orientation of the placenta is different for every mother and the movement induced by the patient's breath during scanning also make it complicated for us to have two exact scans of the same position to compare.

Which are the more appropriate models? We have plotted the histograms of the models in Figure 8. The clear favorite is the stick-ball model, which is aniso-iso, showing the diversity of circulations within the placenta. Coming in second we have the stick-ball-sphere model, where the third "sphere" compartment represents restricted diffusion. This is something also found in (Slator et al., 2018), where there is also evidence of restricted diffusion, which can be a sign of malfunction in the diffusion process. This effect is neither dominant here nor in the latter paper. What we can pick up from the barplot is the fact that the zeppelin-zeppelin (aniso-aniso) model is almost absent in the healthy control, but is significantly higher in the pre-eclampsia one. This is a completely anisotropic model, which can mean that the fluids have less freedom to move around, and thus are less likely to reach their destination. We can expect this malfunction in ill placentas. Though, the number of voxels exhibiting this behavior stays small, so we cannot conclude on this yet. It would be interesting to test this with a more robust optimization method.

Secondly, just like we have done for the ADC and IVIM models, we will take a look at the results obtained for the T_2^* values. They are represented in Figure 9. We can observe that the maps are not too dissimilar from the ones in Figure 4, here they seem to have a better resolution (with some white pixels due to bad fitting with `fminunc`). The high-intensity areas from the maps and the values from the boxplot display the same effect: the T_2^* values are higher for ill placentas. This is expected as organs suffering from pre-eclampsia show a lack of blood oxygenation, as most of our previous references highlight. We confirm once more that T_2^* relaxometry is an efficient way of assessing the sanity of a placenta.

CONCLUSION AND FUTURE DIRECTIONS

As a conclusion, the progress in the acquisition methods of MRI (diffusion-weighted imaging and T_2^* relaxometry) allows us to use novel multi-contrast techniques to map parameters of interest such as the diffusion coefficients and the T_2^* relaxation times, which are proxy to indicate the overall circulation within the placenta as well as the state of oxygenation in the moving fluids (blood, water). We have shown that the T_2^* relaxation time is an appropriate parameter to map: it shows significant differences between healthy and ill placentas, and it does not require complex algorithms: simple T_2^*-ADC or T_2^*-IVIM models are enough to discriminate between two organs. We have also validated the fact that the placenta is indeed a complex organ, full of crossroads and home to many exchanges of nutrients between the fetus and the mother. Such an intricate organ calls for comprehensive models, able to take into account many types of fluid circulations. Our fittings show that we can identify areas of exchange between the uterine wall and the placenta, explaining the microstructure of the latter. These fittings can also give us an insight into the functioning of the placenta: when usual paths are blocked, or when the type of veins/arteries changes; this too can be taken into account when assessing if the placenta suffers from a disease or not.

What we have also highlighted in our findings, is that combining more complex models with T_2^* relaxometry can lead to different results than usual. This exponential pre-factor due to the echo time and relaxation time needs to be handled in more comprehensive models, so that we do not see it only as "signal attenuation" (thus resulting in simpler models being better) but as something that gives us more information about the model. The diversity of placentas makes it hard to have exactly two similar placentas to compare. The complexity of the acquisition (breathing) adds to this effect. There needs to be a more strict model for defining ROIs, so we can have fewer differences when computing the continuum modelling for example (because we use the average signal within the ROI, so different scales of ROI lead to different modellings). Finally, the complexity of the placenta also comes from the fact that we need to follow the veins/arteries throughout different z-scales. We need to come up with models taking into account sets of slices rather than individual ones. We can also think about interpolation models to follow and represent more comprehensively the microstructure of this organ.

REFERENCES

Melbourne, A., Aughwane, R., Sokolska, M., Owen, D., Kendall, G., Flouri, D., Bainbridge, A., Atkinson, D., Deprest, J., Vercauteren, T., David, A., and Ourselin, S. (2018). Separating fetal and maternal placenta circulations using multiparametric mri: Separating placenta circulations using multiparametric mri. *Magnetic Resonance in Medicine*, 81.

Mol, B. W. J., Roberts, C. T., Thangaratinam, S., Magee, L. A., de Groot, C. J. M., and Hofmeyr, G. J. (2016). Pre-eclampsia. *The Lancet*, 387(10022):999–1011.

Panagiotaki, E., Schneider, T., Siow, B., Hall, M., Lythgoe, M., and Alexander, D. (2012). Compartment models of the diffusion mri signal in brain white matter: A taxonomy and comparison. *NeuroImage*, 59:2241–54.

Slator, P., Hutter, J., Palombo, M., Jackson, L., Ho, A., Panagiotaki, E., Chappell, L., Rutherford, M., Hajnal, J., and Daniel, A. (2019). Combined diffusion-relaxometry mri to identify dysfunction in the human placenta. *Magnetic resonance in medicine*.

Slator, P. J., Hutter, J., McCabe, L., Gomes, A. D. S., Price, A. N., Panagiotaki, E., Rutherford, M. A., Hajnal, J. V., and Alexander, D. C. (2018). Placenta microstructure and microcirculation imaging with diffusion mri. *Magnetic Resonance in Medicine*, 80(2):756–766.

TheMathWorksInc. (2022). Matlab version: 9.13.0 (r2022b).